Title

Comparison of chorioretinal layers in rhesus macaques using spectral-domain optical coherence tomography and high-resolution histological sections

Authors

Yiu, Glenn
Wang, Zhe
Munevar, Christian
et al.

Publication Date

2018-03-01

DOI

10.1016/j.exer.2018.01.012

Peer reviewed

HHS Public Access

Author manuscript

Exp Eye Res. Author manuscript; available in PMC 2019 March 01.

Published in final edited form as:

Exp Eye Res. 2018 March ; 168: 69–76. doi:10.1016/j.exer.2018.01.012.

Comparison of Chorioretinal Layers in Rhesus Macaques using Spectral-Domain Optical Coherence Tomography and High-Resolution Histological Sections

Glenn Yiu, MD, PhD[1], **Zhe Wang**[2], **Christian Munevar**[2], **Eric Tieu**[1], **Bradley Shibata**[3], **Brittany Wong**[4], **David Cunefare**[4], **Sina Farsiu, PhD**[4], **Jeffrey Roberts, DVM**[2,5], and **Sara Thomasy, DVM, PhD**[2]

[1]Department of Ophthalmology & Vision Science, University of California, Davis, Sacramento, California

[2]Department of Surgical and Radiological Sciences, School of Veterinary Medicine, University of California, Davis, Davis, California

[3]Department of Cell Biology & Human Anatomy, University of California, Davis, Davis, California

[4]Department of Biomedical Engineering, Duke University, Durham, North Carolina

[5]California National Primate Research Center, Davis, California

Abstract

Nonhuman primates are important preclinical models of retinal diseases because they uniquely possess a macula similar to humans. Ocular imaging technologies such as spectral-domain optical coherence tomography (SD-OCT) allow noninvasive, in vivo measurements of chorioretinal layers with near-histological resolution. However, the boundaries are based on differences in reflectivity, and detailed correlations with histological tissue layers have not been explored in rhesus macaques, which are widely used for biomedical research. Here, we compare the macular anatomy and thickness measurements of chorioretinal layers in rhesus macaque eyes using SD-OCT and high-resolution histological sections. Images were obtained from methylmethacrylate-embedded histological sections of 6 healthy adult rhesus macaques, and compared with SD-OCT images from 6 age-matched animals. Thicknesses of chorioretinal layers were measured across the central 3mm macular region using custom semi-automated or manual software segmentation, and compared between the two modalities. We found that histological sections provide better distinction between the ganglion cell layer (GCL) and inner plexiform layer (IPL) than SD-OCT imaging. The first hyperreflective band between the external limiting membrane (ELM) and retinal pigment epithelium (RPE) appears wider on SD-OCT than the junction between photoreceptor inner and outer segments seen on histology. SD-OCT poorly distinguishes Henle nerve fibers from the outer nuclear layer (ONL), while histology correctly identifies these fibers as part of the outer

Corresponding author: Glenn Yiu, MD, PhD, Department of Ophthalmology & Vision Science, University of California, Davis Eye Center, 4860 Y St., Suite 2400, Sacramento, CA 95817, Phone: 916-734-6602, gyiu@ucdavis.edu.

plexiform layer (OPL). Overall, the GCL, inner nuclear layer (INL), and OPL are significantly thicker on histology, especially at the fovea; while the ONL, choriocapillaris (CC), and outer choroid (OC) are thicker on SD-OCT. Our results show that both SD-OCT and high-resolution histological sections allow reliable measurements of chorioretinal layers in rhesus macaques, with distinct advantages for different sublayers. These findings demonstrate the effects of tissue processing on chorioretinal anatomy, and provide normative values for chorioretinal thickness measurements on SD-OCT for future studies of disease models in these nonhuman primates.

Keywords

optical coherence tomography; histology; retina; rhesus macaque; primate

INTRODUCTION

Nonhuman primates are the only mammals to possess a true macula similar to that of humans, making them ideal animal models for studying foveal development and macular diseases (Cornish et al., 2005; Dawson et al., 1989b; Engel et al., 1988; Francis et al., 2008; Hendrickson and Zhang, 2017; Hope et al., 1992; Sandercoe et al., 2003; Yuodelis and Hendrickson, 1986). Laser-induced choroidal neovascularization may be created to simulate exudative age-related macular degeneration (AMD)(Miller et al., 1990; Miller and Sparrow, 1948; Ryan, 1979), and both rhesus and cynomolgus macaques (Macaca mulatta and Macaca fascicularis), spontaneously develop drusenoid lesions with some features that are clinically similar to those seen in AMD patients (Bellhorn et al., 1981; Dawson et al., 1989a; El-Mofty et al., 1978; Hope et al., 1992; Umeda et al., 2005; Yiu et al., 2017), although nonhuman correlates of more advanced forms of AMD such as choroidal neovascularization and geographic atrophy have never been described. Nonhuman primates also serve as important pre-clinical animal models for novel therapies and drug testing in ophthalmology.

In recent years, spectral-domain optical coherence tomography (SD-OCT) has been increasingly employed as a non-invasive imaging modality to evaluate retinal and choroidal anatomy in human clinical practice and ocular research. Based on low-coherence interferometry using near-infrared light, SD-OCT provides high-resolution cross-sectional images of the retina and choroid due to differential light scattering from individual chorioretinal layers. The differences in reflectivity allow in vivo distinction of the retinal nerve fiber layer (NFL), ganglion cell layer (GCL), inner plexiform layer (IPL), inner nuclear layer (INL), outer plexiform layer (OPL), outer nuclear layer (ONL), external limiting membrane (ELM), as well as the inner and outer segments (IS+OS) of photoreceptors in the retina. Various organelles including melanosomes, lipofuscin, melanolipofuscin granules, and mitochondria account for differential reflectivity of various layers due to the principle of Mie scattering (Wilson et al., 2007; Wilson and Foster, 2007). Melanin granules also accounts partly for the hyperreflectivity of the retinal pigment epithelium (RPE), and may contribute to the reflectance pattern of the underlying choriocapillaris (CC) and outer choroid (OC) as well (Yiu et al., 2016).

The histological correlates of these chorioretinal layers as seen on SD-OCT have been extensively characterized in human subjects, and their normative thickness values have been previously described (Bagci et al., 2008; Chan et al., 2006; Curcio et al., 2011; Grover et al., 2009, 2010; Liu et al., 2011; Sull et al., 2010). Similar studies have also been conducted in laboratory animals including mice and cynomolgus macaques (Anger et al., 2004; Ferguson et al., 2014), but not in rhesus macaques – the most widely-used nonhuman primate in biomedical research. Here, we provide a comprehensive comparison of chorioretinal layers seen on SD-OCT images and high-resolution histological sections in healthy adult rhesus macaques, with the goal of providing a framework for future studies employing this species as a model for retinal or choroidal diseases.

MATERIAL AND METHODS

Subject & Eye Selection

Healthy adult rhesus macaques greater than 6 years of age (roughly equivalent to 18 human years) representing a spectrum of ages through early, middle, and late adult life were selected from animals undergoing routine semiannual physical examinations at the California National Primate Research Center (CNPRC). The CNPRC is accredited by the Association for Assessment and Accreditation of Laboratory Animal Care (AAALAC) International. Our studies using rhesus macaques followed the guidelines of the Association for Research in Vision and Ophthalmology (ARVO) statement for the Use of Animals in Ophthalmic and Vision Research, complied with the National Institutes of Health (NIH) Guide for the Care and Use of Laboratory Animals, and were approved by the University of California, Davis Institutional Animal Care and Use Committee (IACUC). All subjects underwent complete ophthalmic examination including slit-lamp biomicroscopy and dilated fundus biomicroscopy. Animals that showed any retinal or choroidal lesions on clinical examination, such as drusenoid lesions, were excluded from the study.

For histological analysis, cadaveric eyes were collected from rhesus macaques undergoing necropsy for nonocular health issues, with a death-to-preservation time of several minutes (no more than 10 minutes for any eye), and only eyes that had well-preserved chorioretinal anatomy after tissue processing were included. For SD-OCT, age-matched animals with normal ophthalmic examinations were selected to undergo ocular imaging. Only one eye was selected from each animal for analysis, based on the quality of the histological section or SD-OCT image relative to the fellow eye.

For histologic evaluation, the mean age of animals was 16.3 ± 8.7 years (range, 10–27 years), with 4 females and 2 males. 4 were right eyes, and 2 were left eyes. For SD-OCT analysis, the mean age of the selected animals was 18.6 ± 6.5 years (range, 9–28 years), with 4 females and 2 males. Three were right eyes, and 3 were left eyes. The animals selected for SD-OCT were age-matched to those from which histological sections were taken, with no significant difference in mean age ($P = 0.61$) and sex ($P = 1.00$) of animals, or laterality of eyes selected ($P = 0.56$).

Histological Processing

For high-resolution histological sections, entire globes were fixed in 2% paraformaldehyde and 0.5% glutaraldehyde, with a small slit made through the pars plana with a scalpel blade to facilitate penetration of the fixative. Tissues were dehydrated using increasing concentrations of ethanol from 50% to 100%, pre-infiltrated with a 50:50 mixture of ethanol and methylmethacrylate (Technovit®, Kulzer) for 2–3 hours, then infiltrated with methylmethacrylate for a minimum of 24 hours. Serial sections were cut at 1.5 μm thickness through the foveal region using a Leica EM UC6 ultramicrotome, with a horizontal orientation along the optic disc- foveal axis matching the SD-OCT line-scans. The slides were stained with 1% toluidine blue O for 30 seconds, rinsed, dried, and coverslipped (Permount, Fisher). Histological sections were imaged using a 40x objective lens on a Virtual Slide Microscope (VS120-S6-W, Olympus, Tokyo, Japan), at a resolution of 172.51 nm per pixel. For each eye, we performed layer segmentation on images of the histological section closest to the fovea centralis, defined as the center of the foveal depression with lateral displacement of the inner retinal layers, and greatest elongation of the outer segments.

Spectral Domain OCT Imaging

SD-OCT imaging was performed using the Spectralis SD-OCT device (Heidelberg Engineering, Heidelberg, Germany), which has been modified with a flat chin-rest to allow the rhesus monkeys' head to be positioned. We used a wire lid speculum to keep the eyes opened, and applied artificial tears to maintain the tear film on the ocular surface. Animals were monitored by a trained technician and a CNPRC veterinarian while imaging took place. We captured 7 horizontal line scans in a 30º x 5º region centered on the fovea with mean line spacing of 218.7 ± 6.0 μm, in high-resolution mode with 1536 A-scans per B-scan and axial resolution of 3.87 μm per pixel, and using enhanced depth imaging (EDI) mode to optimize visualization of the choroid. The transverse resolution was calibrated based on average corneal curvatures measured for each animal (mean 6.48 ± 0.03 mm) using a corneal topography device (Pentacam HR, Oculus). Twenty-five images were averaged for each B-scan using the Automatic Real-Time (ART) eye-tracking option of the Heidelberg Explorer software (version 1.8.6.0, Heidelberg Engineering). For each eye, we performed image segmentation of the line scan closest to the foveal center, defined as the center of the foveal pit with the greatest separation between the IS-OS (EZ) (Jonnal et al., 2017; Jonnal et al., 2014; Meadway et al., 2013; Staurenghi et al., 2014) and the RPE-Bruchs membrane complex.

Image Segmentation

Digital images of histological sections and SD-OCT images were segmented using the Duke Optical Coherence Tomography Retinal Analysis Program (DOCTRAP, version 62.0), a custom image analysis software designed using MATLAB (Mathworks)(Chiu et al., 2010). For histological sections, layer segmentation was performed manually by two independent graders based on careful evaluation of the chorioretinal structures and anatomic boundaries of digital images on a 27" LCD computer display, viewed at an effective magnification of 500x (Figure 2A). For SD-OCT images, segmentation boundaries were automatically calculated by DOCTRAP using graph-based determination of reflectivity profiles, then

manually refined by the two graders (Figure 2B). Thickness measurements were taken at 0.005mm intervals (601 total positions) along every A-scan across the central 3mm segment centered on the fovea in each horizontal line B-scan, and then averaged across the entire 3mm segment, the central 1mm foveal segment, or the adjacent 1mm parafoveal ring (from 0.5mm to 1.5mm nasal and temporal to the fovea), based on the central circle and inner ring of the Early Treatment Diabetic Retinopathy Study (ETDRS) grid. Measured layers included the NFL, GCL, IPL, INL, OPL, ONL, IS, OS, RPE, CC, and OC, which includes both Sattler's and Haller's layers. These layers were segmented based on the layer definitions defined by the International Nomenclature for Optical Coherence Tomography panel (Staurenghi et al., 2014), including the innermost hyperreflective NFL, hyporeflective GCL, hyperreflective IPL, hyporeflective INL, hyperreflective OPL, hyporeflective ONL, hyporeflective IS myoid layer (measured from the hyperreflective ELM to hyperreflective IS-OS(EZ)), hyporeflective OS layer (measured from the hyperreflective IS-OS(EZ) to the inner boundary of hyperreflective RPE/Bruchs membrane complex), hyperreflective RPE/Bruchs membrane complex layer, thin CC layer of low to moderate reflectivity below RPE/Bruchs complex, and the thick layer of OC (measured from the outer boundary of the CC to the inner boundary of the choroidal-scleral junction). Due to ongoing debate on the origin of the IS-OS(EZ) band on SD-OCT, we employed this terminology despite the consensus nomenclature for the band as EZ. The Henle fiber layer (HFL) is included within the ONL, as it is not easily distinguishable without directional use of OCT (Lujan et al., 2015; Lujan et al., 2011). Total retinal thickness was measured from the internal limiting membrane (ILM) to the outer border of Bruch's membrane (BM). Total choroidal thickness was measured from the outer border of BM to the choroidal-scleral junction as described previously (Vuong et al., 2016; Willoughby et al., 2017; Wong et al., 2017; Yiu et al., 2014).

Statistical Analysis

All measurements reported in this study were calculated from the average measurements of the two graders. Differences in mean age, sex, and eye laterality between the two animal groups were determined by independent samples t-tests and Chi-square tests. Differences in chorioretinal layer thicknesses obtained from histological sections and SD-OCT were compared using two-way analysis of variance (ANOVA) with one-way ANOVA post-hoc testing of each layer. Intergrader repeatability of measurements were assessed using intraclass correlation coefficients (ICC). All statistics were performed using SPSS software (version 22, IBM).

RESULTS

SD-OCT versus Histological Sections

Both SD-OCT and histological sections provided good delineation of the chorioretinal layers, although histology demonstrated superior distinction between the GCL and IPL, while SD-OCT shows a more prominent hyperreflective IS-OS(EZ) than the IS-OS junction seen on histology (Figure 1). SD-OCT poorly distinguishes HFL from the ONL, while histology correctly identifies these fibers as part of the OPL. As expected, the methacrylate-embedded histological sections provide much better cellular-level details. But despite selecting only eyes with well-preserved retinal anatomy, the histological boundaries appear

more distorted than the reflectivity boundaries seen on SD-OCT (Figure 2), likely as a result of tissue handling and sectioning stress. Variance among individual animals was also greater in most chorioretinal layers measured across the central 3 mm segment from histological sections as compared with SD-OCT images, which showed greater uniformity in thickness measurements between different animals as suggested by the lower standard deviation of measurements (Table 1).

Histological sections and SD-OCT showed an overall difference in chorioretinal layer measurements ($P = 0.017$). Total retinal thickness averaged across the central macula showed no significant differences between the two modalities ($P = 0.136$), but total choroidal thickness was 46.3% thinner on histology (105.3 ± 18.6 μm vs. 196.0 ± 20.2 μm; $P < 0.001$), possibly demonstrating the greater susceptibility of vascular tissues to shrinkage with histological processing compared with neurosensory retinal tissue, and also the lower reliability of choroidal thickness measurements from SD-OCT. When comparing individual retinal and choroidal layers, several retinal layers including the GCL, INL, and OPL appeared significantly thicker on histological sections, while the ONL and choroidal layers (CC and OC) were thicker on SD-OCT (Figure 3). For retinal layers that showed a significant difference between the two modalities, the measurement differences were more pronounced in the central 1mm of the fovea, compared to the outer 1mm parafoveal ring, while histological shrinkage in CC and OC thickness was more evenly distributed across the central macula (Table 2, Figure 3).

Measurement Reliability

Intergrader repeatability was good between the two graders, but was generally superior for histological sections than SD-OCT (Table 3), likely due to better distinction of retinal layers and higher resolution of the digital images from histology versus SD-OCT (172.5 nm vs. 3.87 μm per pixel). For measurements from SD-OCT images, repeatability of thinner retinal layers such as the photoreceptor OS and RPE were lower, while IS measurements produced a paradoxically negative ICC value, likely due to low between-subject variance, and thus cannot be interpreted from our sample according to James and colleagues (James et al., 1984). Consistent with prior studies, the repeatability of choroidal thickness measurements were lower than those from retinal layers on SD-OCT, which may be attributed to the poorer delineation of the choroidal-scleral junction in these pigmented animals (Yiu et al., 2016).

DISCUSSION

Nonhuman primates are important animal models for studying human ophthalmic diseases and therapies due to their similar ocular anatomy and the presence of a macula resembling those in humans (Bellhorn et al., 1981; Bumsted and Hendrickson, 1999; Dawson et al., 1989a; Dawson et al., 1989b; El-Mofty et al., 1978; Engel et al., 1988; Feeney-Burns et al., 1981; Fine and Kwapien, 1978; Francis et al., 2008; Hendrickson and Zhang, 2017; Hendrickson, 1994; Hope et al., 1992; Monaco and Wormington, 1990; Olin et al., 1995; Provis et al., 2000; Stafford et al., 1984; Yiu et al., 2017; Yiu et al., 2016). The expanding use of SD-OCT for clinical and research applications allows unprecedented in vivo visualization of retinal and choroidal anatomy in both humans and macaques with near-

histological resolution (Keane et al., 2012). This noninvasive imaging modality allows structural changes to be monitored over time, with high levels of reproducibility.

However, chorioretinal boundaries on SD-OCT are distinguished by differences in tissue reflectivity rather than tissue or cell types, and thus may over-emphasize or de-emphasize certain anatomic boundaries based on the light-scattering property of the interface. For example, the contrast between GCL and IPL are low, making these layers difficult to distinguish from each other on OCT, while the hyperreflective bands seen in the outer retinal layers demonstrate higher contrast on OCT than the anatomic boundaries seen on histological sections using toluidine staining. The origin of the first hyperreflective band between the ELM and the RPE on SD-OCT has been debated as possibly representing the inner segment ellipsoid zone (EZ)(Spaide and Curcio, 2011), although evidence from single-cell measurements using adaptive optics-OCT suggests that it is more properly ascribed to the IS-OS junction of photoreceptors (Jonnal et al., 2017; Jonnal et al., 2014; Meadway et al., 2013). SD-OCT also poorly distinguishes HFL from the ONL, even though they are anatomically part of the OPL, likely due to the oblique orientation of the fibers relative to the OCT light path which scatters light away from the pupillary axis (Lujan et al., 2011). This phenomenon explains the increased thickness of the ONL seen on SD-OCT compared with the thicker OPL on histology in our study, and could be mitigated with the use of directional OCT (Lujan et al., 2015). In addition, the axial scaling of the OCT signal may not be completely linear across the different chorioretinal layers. Since the signal depends in part on the refractive index of tissues (Cheng and Liu, 2010; Drexler et al., 2001; Zhou et al., 2013), layers that are rich in lipids such as the IS ellipsoid or OS may refract light and scale differently than layers that have more aqueous components (Hoang et al., 2002; Rowe et al., 1996). Further, the melanosomes that in part confer the hyperreflective property of the RPE and OC in macaques also allow better distinction of the CC, attenuate the light signal in the OC, and reduce the delineation of the choroidal-scleral junction as compared with humans, where the choroid is less pigmented (Yiu et al., 2016). These effects may explain the higher reliability of choriocapillaris measurements and lower reliability of choroidal thickness measurements, and cause the choroid to appear artificially thicker on SD-OCT. Finally, our reliability measures suggest that SD-OCT measurements are overall less reliable for thinner outer retinal layers that approach the axial resolution of the system, and for choroidal vascular layers that are difficult to visualize even with the use of enhanced-depth imaging mode. Some experts have advocated for utilizing raw OCT images to measure true retinal layer thicknesses to avoid potential distortion from logarithmic contrast enhancement (Ross et al., 2015; Spaide and Curcio, 2011). However, we note that the logarithmic function mitigates the exponentially-dominated process of depth-dependent loss of OCT signal (DuBose et al., 2018). Further research may provide additional insight into optimizing the accuracy of chorioretinal layer thickness measurements from OCT images.

Histological analysis provides detailed visualization of retinal structures, and may be combined with various tissue stains and molecular probes to anatomically localize molecular and cellular changes that exceed the capability of most ocular imaging systems to date. Measurements of chorioretinal layers are also highly reproducible, especially for thinner chorioretinal layers such as the NFL, IS, OS, RPE, and CC, where repeatability of measurements from histology are vastly superior to those on OCT. Yet, tissue processing for

histology may result in dehydration and shrinkage, and distortion of certain chorioretinal layers or retinal contour due to sectioning stress. These variations likely account for the greater standard deviation of values measured from histology compared with OCT. Of note, the contour of the foveal pit appears more steep on histology than on SD-OCT, which may indicate greater tissue shrinkage along the plane of the neurosensory retina than along the cross-sectional axis. Our use of methylmethacrylate embedding agent enables better preservation of the retinal anatomy to some degree, but likely still results in less accurate centration and orthogonality of transecting the fovea centralis compared with SD-OCT imaging. This notion is supported by the thicker inner retinal layers seen on histology, and the finding that measurement differences between the two modalities were most pronounced at the fovea. Measurement of vascular structures from histological sections are even less accurate, with nearly 50% shrinkage of choroidal layers likely from loss of intravascular pressure and collapse of the choroidal vessel lumina, although SD-OCT imaging also has limited reliability for measuring choroidal thickness in heavily-pigmented animals like macaques (Vuong et al., 2016; Yiu et al., 2016). Despite our rapid death-to-preservation time of several minutes, additional steps for tissue preservation such as animal perfusion may better preserve choroidal vascular integrity for thickness measurements, and tissue osmication can stabilize structures that are rich in lipid membranes, such as photoreceptor outer segments. Use of a more rigid epoxy embedding agent may provide better anatomic preservation for future studies of finer pathologic features such as drusenoid lesions.

Despite these limitations, both SD-OCT and histology remain important and complementary tools in ophthalmic research with nonhuman primates. Our study provides normative values for chorioretinal layer thicknesses measured from both SD-OCT and histological sections from healthy eyes of rhesus macaques, and serves as reference for future biomedical ocular research in this species. In particular, the measurements of thicker chorioretinal layers on SD-OCT are highly reproducible using semi-automated segmentation software that has been validated in human clinical trials (Farsiu et al., 2014), although the reliability of thinner layers that approach the axial resolution of the SD-OCT system are lower. The use of these segmentation methods for histological sections further improves the precision and reproducibility of histological analyses, despite the inherent variability of tissue processing. Our study is limited by the use of different sets of animals for histology and SD-OCT, although we noted relatively small interindividual variability between animals, particularly on OCT measurements. Importantly, the chorioretinal layer measurements here are comparable to those of similar studies conducted in humans and cynomolgus macaques, which have similar ocular dimensions as rhesus monkeys (Anger et al., 2004; Curcio et al., 2011). These similarities further support the use of rhesus macaques and other nonhuman primates as animal models for human retinal diseases.

Acknowledgments

We thank Dr. Philip Kass at UC Davis School of Veterinary Medicine for assistance with statistical analyses, Iris Molhoff and Dr. Kevin Keel for image capture using virtual slide microscopy, and Yinwen Wang for assistance with image analysis. Histological processing was performed with support from histology core facilities under the Vision Research Core Grant NIH P30 EY12576. The use of rhesus macaques was supported by the California National Primate Research Center base grant NIH P510D011107. GY is supported by NIH K08 EY026101, the E. Matilda Ziegler Foundation for the Blind, Barr Foundation for Retinal Research, Alcon Research Institute, and the ARVO Foundation. CM and ZW are supported by the School of Veterinary Medicine Endowment Funds. SF is supported

by NIH P30 EY005722. ST is supported by NIH K08 EY021142. No funding organizations had any role in the design or conduct of this research. The content is solely the responsibility of the authors and does not necessarily represent the official views of the funding agencies.

References

Anger EM, Unterhuber A, Hermann B, Sattmann H, Schubert C, Morgan JE, Cowey A, Ahnelt PK, Drexler W. Ultrahigh resolution optical coherence tomography of the monkey fovea. Identification of retinal sublayers by correlation with semithin histology sections. Exp Eye Res. 2004; 78:1117–1125. [PubMed: 15109918]

Bagci AM, Shahidi M, Ansari R, Blair M, Blair NP, Zelkha R. Thickness profiles of retinal layers by optical coherence tomography image segmentation. Am J Ophthalmol. 2008; 146:679–687. [PubMed: 18707672]

Bellhorn RW, King CD, Aguirre GD, Ripps H, Siegel IM, Tsai HC. Pigmentary abnormalities of the macula in rhesus monkeys: clinical observations. Investigative ophthalmology & visual science. 1981; 21:771–781. [PubMed: 7309433]

Bumsted K, Hendrickson A. Distribution and development of short-wavelength cones differ between Macaca monkey and human fovea. J Comp Neurol. 1999; 403:502–516. [PubMed: 9888315]

Chan A, Duker JS, Ko TH, Fujimoto JG, Schuman JS. Normal macular thickness measurements in healthy eyes using Stratus optical coherence tomography. Arch Ophthalmol. 2006; 124:193–198. [PubMed: 16476888]

Cheng HC, Liu YC. Simultaneous measurement of group refractive index and thickness of optical samples using optical coherence tomography. Appl Opt. 2010; 49:790–797. [PubMed: 20154745]

Chiu SJ, Li XT, Nicholas P, Toth CA, Izatt JA, Farsiu S. Automatic segmentation of seven retinal layers in SDOCT images congruent with expert manual segmentation. Optics express. 2010; 18:19413–19428. [PubMed: 20940837]

Cornish EE, Madigan MC, Natoli R, Hales A, Hendrickson AE, Provis JM. Gradients of cone differentiation and FGF expression during development of the foveal depression in macaque retina. Vis Neurosci. 2005; 22:447–459. [PubMed: 16212702]

Curcio CA, Messinger JD, Sloan KR, Mitra A, McGwin G, Spaide RF. Human chorioretinal layer thicknesses measured in macula-wide, high-resolution histologic sections. Investigative ophthalmology & visual science. 2011; 52:3943–3954. [PubMed: 21421869]

Dawson WW, Engel HM, Hope GM, Kessler MJ, Ulshafer RJ. Adult-onset macular degeneration in the Cayo Santiago macaques. P R Health Sci J. 1989a; 8:111–115. [PubMed: 2780951]

Dawson WW, Ulshafer RJ, Engel HM, Hope GM, Kessler MJ. Macular disease in related rhesus monkeys. Doc Ophthalmol. 1989b; 71:253–263. [PubMed: 2789127]

Drexler W, Morgner U, Ghanta RK, Kartner FX, Schuman JS, Fujimoto JG. Ultrahigh-resolution ophthalmic optical coherence tomography. Nat Med. 2001; 7:502–507. [PubMed: 11283681]

DuBose TB, Cunefare D, Cole E, Milanfar P, Izatt JA, Farsiu S. Statistical Models of Signal and Noise and Fundamental Limits of Segmentation Accuracy in Retinal Optical Coherence Tomography. IEEE Transactions on Medical Imaging. 2018 In Press.

El-Mofty A, Gouras P, Eisner G, Balazs EA. Macular degeneration in rhesus monkey (Macaca mulatta). Exp Eye Res. 1978; 27:499–502. [PubMed: 103738]

Engel HM, Dawson WW, Ulshafer RJ, Hines MW, Kessler MJ. Degenerative changes in maculas of rhesus monkeys. Ophthalmologica. 1988; 196:143–150. [PubMed: 3405585]

Farsiu S, Chiu SJ, O'Connell RV, Folgar FA, Yuan E, Izatt JA, Toth CA. Age-Related Eye Disease Study 2 Ancillary Spectral Domain Optical Coherence Tomography Study G. Quantitative classification of eyes with and without intermediate age-related macular degeneration using optical coherence tomography. Ophthalmology. 2014; 121:162–172. [PubMed: 23993787]

Feeney-Burns L, Malinow R, Klein ML, Neuringer M. Maculopathy in cynomolgus monkeys. A correlated fluorescein angiographic and ultrastructural study. Arch Ophthalmol. 1981; 99:664–672. [PubMed: 7224938]

Ferguson LR, Grover S, Dominguez JM 2nd, Balaiya S, Chalam KV. Retinal thickness measurement obtained with spectral domain optical coherence tomography assisted optical biopsy accurately correlates with ex vivo histology. PloS one. 2014; 9:e111203. [PubMed: 25360629]

Fine BS, Kwapien RP. Pigment epithelial windows and drusen: an animal model. Investigative ophthalmology & visual science. 1978; 17:1059–1068. [PubMed: 100467]

Francis PJ, Appukuttan B, Simmons E, Landauer N, Stoddard J, Hamon S, Ott J, Ferguson B, Klein M, Stout JT, Neuringer M. Rhesus monkeys and humans share common susceptibility genes for age-related macular disease. Hum Mol Genet. 2008; 17:2673–2680. [PubMed: 18535016]

Grover S, Murthy RK, Brar VS, Chalam KV. Normative data for macular thickness by high-definition spectral-domain optical coherence tomography (spectralis). Am J Ophthalmol. 2009; 148:266–271. [PubMed: 19427616]

Grover S, Murthy RK, Brar VS, Chalam KV. Comparison of retinal thickness in normal eyes using Stratus and Spectralis optical coherence tomography. Investigative ophthalmology & visual science. 2010; 51:2644–2647. [PubMed: 20007831]

Hendrickson A, Zhang C. Development of cone photoreceptors and their synapses in the human and monkey fovea. J Comp Neurol. 2017

Hendrickson AE. Primate foveal development: a microcosm of current questions in neurobiology. Investigative ophthalmology & visual science. 1994; 35:3129–3133. [PubMed: 8045707]

Hoang QV, Linsenmeier RA, Chung CK, Curcio CA. Photoreceptor inner segments in monkey and human retina: mitochondrial density, optics, and regional variation. Vis Neurosci. 2002; 19:395–407. [PubMed: 12511073]

Hope GM, Dawson WW, Engel HM, Ulshafer RJ, Kessler MJ, Sherwood MB. A primate model for age related macular drusen. Br J Ophthalmol. 1992; 76:11–16. [PubMed: 1739683]

James LR, Demaree RG, Wolf G. Estimating within-group interarter reliability with and without response bias. Journal of Applied Psychology. 1984; 69:85–98.

Jonnal RS, Gorczynska I, Migacz JV, Azimipour M, Zawadzki RJ, Werner JS. The Properties of Outer Retinal Band Three Investigated With Adaptive-Optics Optical Coherence Tomography. Investigative ophthalmology & visual science. 2017; 58:4559–4568. [PubMed: 28877320]

Jonnal RS, Kocaoglu OP, Zawadzki RJ, Lee SH, Werner JS, Miller DT. The cellular origins of the outer retinal bands in optical coherence tomography images. Investigative ophthalmology & visual science. 2014; 55:7904–7918. [PubMed: 25324288]

Keane PA, Patel PJ, Liakopoulos S, Heussen FM, Sadda SR, Tufail A. Evaluation of age-related macular degeneration with optical coherence tomography. Surv Ophthalmol. 2012; 57:389–414. [PubMed: 22898648]

Liu YY, Ishikawa H, Chen M, Wollstein G, Duker JS, Fujimoto JG, Schuman JS, Rehg JM. Computerized macular pathology diagnosis in spectral domain optical coherence tomography scans based on multiscale texture and shape features. Investigative ophthalmology & visual science. 2011; 52:8316–8322. [PubMed: 21911579]

Lujan BJ, Roorda A, Croskrey JA, Dubis AM, Cooper RF, Bayabo JK, Duncan JL, Antony BJ, Carroll J. Directional Optical Coherence Tomography Provides Accurate Outer Nuclear Layer and Henle Fiber Layer Measurements. Retina. 2015; 35:1511–1520. [PubMed: 25829348]

Lujan BJ, Roorda A, Knighton RW, Carroll J. Revealing Henle's fiber layer using spectral domain optical coherence tomography. Investigative ophthalmology & visual science. 2011; 52:1486–1492. [PubMed: 21071737]

Meadway A, Girkin CA, Zhang Y. A dual-modal retinal imaging system with adaptive optics. Optics express. 2013; 21:29792–29807. [PubMed: 24514529]

Miller H, Miller B, Ishibashi T, Ryan SJ. Pathogenesis of laser-induced choroidal subretinal neovascularization. Investigative ophthalmology & visual science. 1990; 31:899–908. [PubMed: 1692312]

Miller RP, Sparrow TD. The pathogenesis, diagnosis, and treatment of varicose veins and varicose ulcers; analysis of 200 cases treated by upper saphenous ligation. N C Med J. 1948; 9:574–579. [PubMed: 18890721]

Monaco WA, Wormington CM. The rhesus monkey as an animal model for age-related maculopathy. Optometry and vision science : official publication of the American Academy of Optometry. 1990; 67:532–537. [PubMed: 2402402]

Olin KL, Morse LS, Murphy C, Paul-Murphy J, Line S, Bellhorn RW, Hjelmeland LM, Keen CL. Trace element status and free radical defense in elderly rhesus macaques (Macaca mulatta) with macular drusen. Proc Soc Exp Biol Med. 1995; 208:370–377. [PubMed: 7700885]

Provis JM, Sandercoe T, Hendrickson AE. Astrocytes and blood vessels define the foveal rim during primate retinal development. Investigative ophthalmology & visual science. 2000; 41:2827–2836. [PubMed: 10967034]

Ross DH, Clark ME, Godara P, Huisingh C, McGwin G, Owsley C, Litts KM, Spaide RF, Sloan KR, Curcio CA. RefMoB, a Reflectivity Feature Model-Based Automated Method for Measuring Four Outer Retinal Hyperreflective Bands in Optical Coherence Tomography. Investigative ophthalmology & visual science. 2015; 56:4166–4176. [PubMed: 26132776]

Rowe MP, Corless JM, Engheta M, Pugh ENJ. Scanning interferometry of sunfish cones. I. Longitudinal variation in single-cone refractive index. J Opt Soc Am A. 1996:13.

Ryan SJ. The development of an experimental model of subretinal neovascularization in disciform macular degeneration. Transactions of the American Ophthalmological Society. 1979; 77:707–745. [PubMed: 94717]

Sandercoe TM, Geller SF, Hendrickson AE, Stone J, Provis JM. VEGF expression by ganglion cells in central retina before formation of the foveal depression in monkey retina: evidence of developmental hypoxia. J Comp Neurol. 2003; 462:42–54. [PubMed: 12761823]

Spaide RF, Curcio CA. Anatomical correlates to the bands seen in the outer retina by optical coherence tomography: literature review and model. Retina. 2011; 31:1609–1619. [PubMed: 21844839]

Stafford TJ, Anness SH, Fine BS. Spontaneous degenerative maculopathy in the monkey. Ophthalmology. 1984; 91:513–521. [PubMed: 6204261]

Staurenghi G, Sadda S, Chakravarthy U, Spaide RF. International Nomenclature for Optical Coherence Tomography P. Proposed lexicon for anatomic landmarks in normal posterior segment spectral-domain optical coherence tomography: the IN*OCT consensus. Ophthalmology. 2014; 121:1572–1578. [PubMed: 24755005]

Sull AC, Vuong LN, Price LL, Srinivasan VJ, Gorczynska I, Fujimoto JG, Schuman JS, Duker JS. Comparison of spectral/Fourier domain optical coherence tomography instruments for assessment of normal macular thickness. Retina. 2010; 30:235–245. [PubMed: 19952997]

Umeda S, Suzuki MT, Okamoto H, Ono F, Mizota A, Terao K, Yoshikawa Y, Tanaka Y, Iwata T. Molecular composition of drusen and possible involvement of anti-retinal autoimmunity in two different forms of macular degeneration in cynomolgus monkey (Macaca fascicularis). FASEB J. 2005; 19:1683–1685. [PubMed: 16099945]

Vuong VS, Moisseiev E, Cunefare D, Farsiu S, Moshiri A, Yiu G. Repeatability of Choroidal Thickness Measurements on Enhanced Depth Imaging Optical Coherence Tomography Using Different Posterior Boundaries. Am J Ophthalmol. 2016; 169:104–112. [PubMed: 27345731]

Willoughby AS, Vuong VS, Cunefare D, Farsiu S, Noronha G, Danis RP, Yiu G. Choroidal Changes After Suprachoroidal Injection of Triamcinolone Acetonide in Eyes With Macular Edema Secondary to Retinal Vein Occlusion. Am J Ophthalmol. 2017

Wilson JD, Cottrell WJ, Foster TH. Index-of-refraction-dependent subcellular light scattering observed with organelle-specific dyes. Journal of biomedical optics. 2007; 12:014010. [PubMed: 17343485]

Wilson JD, Foster TH. Characterization of lysosomal contribution to whole-cell light scattering by organelle ablation. Journal of biomedical optics. 2007; 12:030503. [PubMed: 17614706]

Wong SS, Vuong VS, Cunefare D, Farsiu S, Moshiri A, Yiu G. Macular Fluid Reduces Reproducibility of Choroidal Thickness Measurements on Enhanced Depth Optical Coherence Tomography. Am J Ophthalmol. 2017; 184:108–114. [PubMed: 29038011]

Yiu G, Pecen P, Sarin N, Chiu SJ, Farsiu S, Mruthyunjaya P, Toth CA. Characterization of the choroid-scleral junction and suprachoroidal layer in healthy individuals on enhanced-depth imaging optical coherence tomography. JAMA Ophthalmol. 2014; 132:174–181. [PubMed: 24336985]

Yiu G, Tieu E, Munevar C, Wong B, Cunefare D, Farsiu S, Garzel L, Roberts J, Thomasy SM. In Vivo Multimodal Imaging of Drusenoid Lesions in Rhesus Macaques. Sci Rep. 2017; 7:15013. [PubMed: 29101353]

Yiu G, Vuong VS, Oltjen S, Cunefare D, Farsiu S, Garzel L, Roberts J, Thomasy SM. Effect of Uveal Melanocytes on Choroidal Morphology in Rhesus Macaques and Humans on Enhanced-Depth Imaging Optical Coherence Tomography. Investigative ophthalmology & visual science. 2016; 57:5764–5771. [PubMed: 27792810]

Yuodelis C, Hendrickson A. A qualitative and quantitative analysis of the human fovea during development. Vision Res. 1986; 26:847–855. [PubMed: 3750868]

Zhou Y, Chan KK, Lai T, Tang S. Characterizing refractive index and thickness of biological tissues using combined multiphoton microscopy and optical coherence tomography. Biomedical optics express. 2013; 4:38–50. [PubMed: 23304646]

Highlights

- Both SD-OCT and histology allow reproducible measurements of chorioretinal layers using software segmentation
- Histology is superior to SD-OCT for distinguishing the ganglion cell layer from inner plexiform layer, and Henle nerve fibers from outer nuclear layer.
- Histological sections show greater cellular details, but suffers from distortions from tissue processing, particularly in choroidal layers.

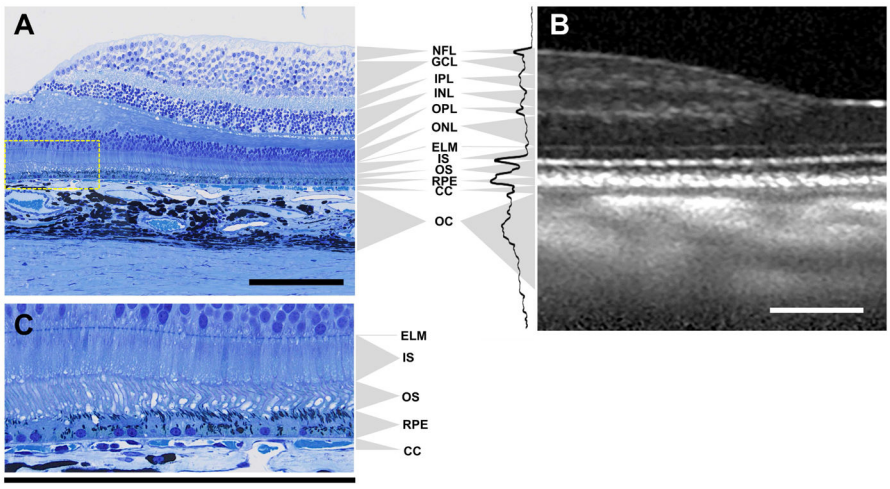

Figure 1.

Comparison of high-resolution histological sections and spectral domain-optical coherence tomography (SD-OCT) images of a normal eye in an adult rhesus macaque. Histological sections stained with toluidine O (A) demonstrate individual chorioretinal layers corresponding to those seen on an SD-OCT image (B) along with the reflectivity profile measured from 10 adjacent A-scans at the left-hand side of panel B. Higher magnification (C) of the area outlined in panel A (yellow dashed box) shows greater details of the outer retinal and inner choroidal layers. The photoreceptor outer segments can be seen to overlap slightly with the RPE apical processes. The vacuolization of some cone pedicles in the outer plexiform layer and also some outer segments is artifact. Scale bars: 200 μm. Abbreviations: NFL, nerve fiber layer; GCL, ganglion cell layer; IPL, inner plexiform layer; INL, inner nuclear layer; OPL, outer plexiform layer; ONL, outer nuclear layer; ELM, external limiting membrane; IS, photoreceptor inner segments; OS, photoreceptor outer segments; RPE, retinal pigment epithelium; CC, choriocapillaris; OC, outer choroid.

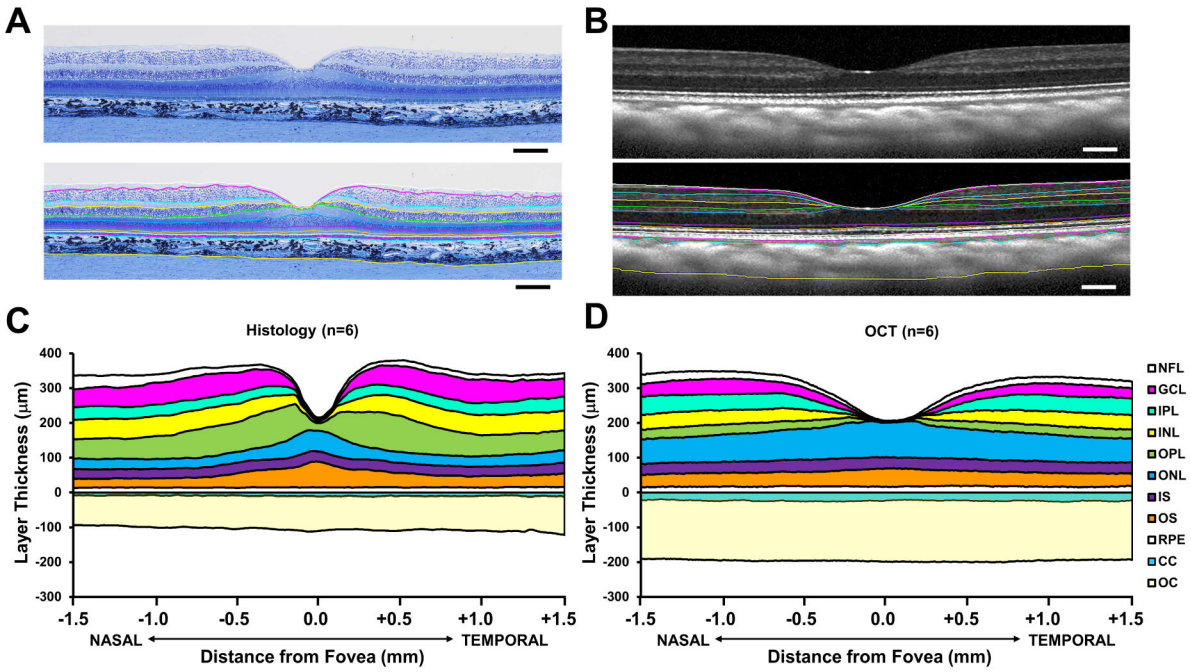

Figure 2.

Image segmentation and thickness of chorioretinal layers in rhesus macaques. A high-resolution histological section (A) and SD-OCT image (B) of normal maculae from adult rhesus macaque eyes before (top panels) and after (bottom panels) image segmentation. Retinal and choroidal thickness measurements across the central 3 mm segment around the fovea, as well as individual sublayers are compared between histology (C) and SD-OCT (D). Cumulative thicknesses are measured from Bruch's membrane, which is designated at zero. Scale bars: 200 μm. The line graphs in (C) and (D) are not drawn to the same scale as the SD-OCT and histological images in (A) and (B). Abbreviations: NFL, nerve fiber layer; GCL, ganglion cell layer; IPL, inner plexiform layer; INL, inner nuclear layer; OPL, outer plexiform layer; ONL, outer nuclear layer; ELM, external limiting membrane; IS, photoreceptor inner segments; OS, photoreceptor outer segments; RPE, retinal pigment epithelium; CC, choriocapillaris; OC, outer choroid.

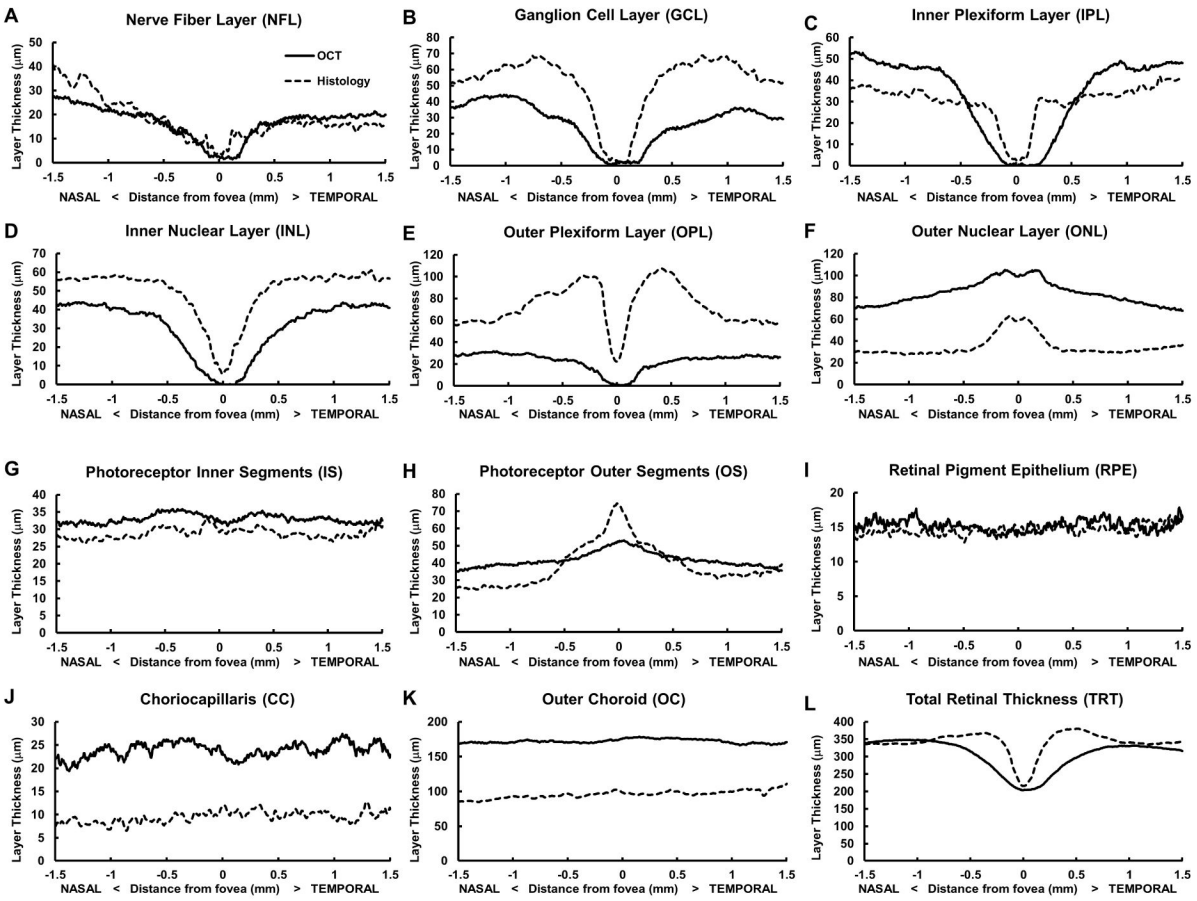

Figure 3.

Comparison of chorioretinal layer thicknesses measured from high-resolution histological sections and SD-OCT across the central 3 mm segment around the fovea. Topographic plots of the nerve fiber layer (A), ganglion cell layer (B), inner plexiform layer (C), inner nuclear layer (D), outer plexiform layer (E); outer nuclear layer (F); photoreceptor inner segments (G); photoreceptor outer segments (H), retinal pigment epithelium (I), choriocapillaris (J), and outer choroid (K), along with total retinal thickness (L) show differences in measurements taken from histological sections (solid lines) and SD-OCT images (dashed lines).

Table 1

Comparison of chorioretinal thicknesses measured on SD-OCT and Histology

	SD-OCT (μm)	Histology (μm)	Difference (%)	P-value
Total retinal thickness (TRT) *	304.8 ± 19.1	340.1 ± 49.8	+11.5	0.136
Nerve fiber layer (NFL)	16.8 ± 1.9	17.9 ± 5.7	+6.5	0.658
Ganglion cell layer (GCL)	27.0 ± 3.5	51.6 ± 11.1	+91.1	<0.001
Inner plexiform layer (IPL)	33.6 ± 4.6	30.2 ± 4.6	−10.1	0.221
Inner nuclear layer (INL)	30.7 ± 4.4	49.5 ± 4.9	+61.2	<0.001
Outer plexiform layer (OPL)	22.5 ± 3.7	73.4 ± 24.4	+226.2	<0.001
Outer nuclear layer (ONL)	84.0 ± 10.4	35.2 ± 2.6	−58.1	<0.001
Photoreceptor inner segments (IS)	33.0 ± 1.1	28.8 ± 6.1	−12.7	0.125
Photoreceptor outer segments (OS)	41.9 ± 2.5	39.0 ± 20.0	−6.9	0.724
Retinal pigment epithelium (RPE)	15.3 ± 2.3	14.6 ± 3.0	−4.6	0.676
Choriocapillaris (CC)	23.9 ± 4.4	9.5 ± 4.0	−60.3	<0.001
Outer choroid (OC)	172.1 ± 20.1	95.8 ± 17.1	−44.3	<0.001
Total choroidal thickness (TCT)	196.0 ± 20.2	105.3 ± 18.6	−46.3	<0.001
Overall				0.017

* All thickness measurements presented as mean ± standard deviation

Table 2

Comparison of chorioretinal thicknesses at the fovea and parafovea as measured on SD-OCT and Histology

	Foveal			Parafoveal		
	SD-OCT (μm)	**Histology (μm)**	**P-value**	**SD-OCT (μm)**	**Histology (μm)**	**P-value**
Nerve fiber layer (NFL) *	9.2 ± 2.3	10.6 ± 4.7	0.51	20.6 ± 2.9	21.6 ± 6.5	0.75
Ganglion cell layer (GCL)	12.1 ± 3.7	33.7 ± 9.8	<0.001	34.5 ± 4.1	60.6 ± 12.3	0.001
Inner plexiform layer (IPL)	10.6 ± 5.1	21.7 ± 4.1	0.002	45.3 ± 4.9	34.4 ± 5.4	0.005
Inner nuclear layer (INL)	12.5 ± 4.6	35.1 ± 4.5	<0.001	39.8 ± 4.9	56.7 ± 8.2	0.001
Outer plexiform layer (OPL)	13.5 ± 5.9	83.0 ± 21.0	<0.001	27.1 ± 2.9	68.6 ± 26.7	0.004
Outer nuclear layer (ONL)	96.5 ± 15.3	44.5 ± 2.6	<0.001	77.6 ± 8.5	30.4 ± 3.3	<0.001
Photoreceptor inner segments (IS)	34.0 ± 1.9	30.0 ± 6.1	0.16	32.5 ± 1.4	28.1 ± 6.2	0.12
Photoreceptor outer segments (OS)	47.0 ± 3.2	54.0 ± 34.9	0.63	39.4 ± 2.6	31.3 ± 13.1	0.17
Retinal pigment epithelium (RPE)	14.7 ± 2.8	14.7 ± 3.3	0.99	15.5 ± 2.1	14.6 ± 2.8	0.51
Choriocapillaris (CC)	23.8 ± 5.5	10.2 ± 4.5	0.001	24.0 ± 4.3	9.2 ± 3.8	<0.001
Outer choroid (OC)	174.1 ± 18.2	96.9 ± 16.0	<0.001	171.0 ± 21.3	95.2 ± 18.0	<0.001

* All thickness measurements presented as mean ± standard deviation

Table 3

Reproducibility of chorioretinal thicknesses measured from SD-OCT and Histology

	SD-OCT ICC*	Histology ICC*
Total retinal thickness (TRT)	0.999	1.000
Nerve fiber layer (NFL)	0.816	0.975
Ganglion cell layer (GCL)	0.895	0.997
Inner plexiform layer (IPL)	0.974	0.993
Inner nuclear layer (INL)	0.997	0.993
Outer plexiform layer (OPL)	0.973	1.000
Outer nuclear layer (ONL)	0.996	0.977
Photoreceptor inner segments (IS)	−0.511	0.983
Photoreceptor outer segments (OS)	0.733	0.998
Retinal pigment epithelium (RPE)	0.622	0.936
Choriocapillaris (CC)	0.966	0.944
Outer choroid (OC)	0.212	0.999
Total choroidal thickness (TCT)	0.274	0.999

*Intraclass correlations